Liquid phase epitaxy growth and structural characterization of highly-doped Er3+:LiYF4 thin films

Liza Basyrova, Gurvan Brasse, Pavel Loiko, Clara Grygiel, Rosa Maria Solé, Magdalena Aguiló, Francesc Díaz, Xavier Mateos, Abdelmjid Benayad, Jean-Louis Doualan, et al.

▶ **To cite this version:**

Liza Basyrova, Gurvan Brasse, Pavel Loiko, Clara Grygiel, Rosa Maria Solé, et al.. Liquid phase epitaxy growth and structural characterization of highly-doped Er3+:LiYF4 thin films. Optical Materials, 2022, 132, pp.112574. 10.1016/j.optmat.2022.112574 . hal-04211119

HAL Id: hal-04211119
https://hal.science/hal-04211119

Submitted on 1 Nov 2023

HAL is a multi-disciplinary open access archive for the deposit and dissemination of scientific research documents, whether they are published or not. The documents may come from teaching and research institutions in France or abroad, or from public or private research centers.

L'archive ouverte pluridisciplinaire **HAL**, est destinée au dépôt et à la diffusion de documents scientifiques de niveau recherche, publiés ou non, émanant des établissements d'enseignement et de recherche français ou étrangers, des laboratoires publics ou privés.

Liquid Phase Epitaxy growth and structural characterization of highly-doped Er^{3+}:$LiYF_4$ thin films

Liza Basyrova[a], Gurvan Brasse[a], Pavel Loiko[a], Clara Grygiel[a], Rosa Maria Solé[b], Magdalena Aguiló[b], Francesc Díaz[b], Xavier Mateos[b,#], Abdelmjid Benayad[a], Jean-Louis Doualan[a], and Patrice Camy[a,*]

[a]*Centre de Recherche sur les Ions, les Matériaux et la Photonique (CIMAP), UMR 6252 CEA-CNRS-ENSICAEN, Université de Caen Normandie, 6 Boulevard Maréchal Juin, 14050 Caen Cedex 4, France*
[b]*Universitat Rovira i Virgili (URV), Física i Cristal·lografia de Materials i Nanomaterials (FiCMA-FiCNA), Marcel.li Domingo 1, 43007 Tarragona, Spain*
[#]*Serra Húnter Fellow, Spain*
**Corresponding author, e-mail: patrice.camy@ensicaen.fr*

Abstract. Single-crystalline layers of $LiYF_4$, singly doped with Er^{3+} ions and codoped with Er^{3+},Gd^{3+} ions are grown on (001) oriented undoped bulk $LiYF_4$ substrates by Liquid Phase Epitaxy using LiF as a solvent. For the starting composition 73 LiF – 27 REF_3 mol% (RE = Y, Er, Gd), the onset of crystallization is about 746 °C. The effect of apparent supercooling on the growth behavior is studied indicating an optimum value of 0.5 °C. Layers of 30 – 90 μm in thickness are obtained corresponding to a growth rate of 0.8 – 1.6 ± 0.5 μm/min. The morphology, structure and composition of the layers are studied. The layers exhibit tetragonal structure (sp. gr. $I4_1/a$) and small lattice mismatch with respect to the substrate. The segregation coefficient for Er^{3+} ions is close to unity. Intense mid-infrared luminescence of Er^{3+} ions at ~2.8 μm is observed from the layers, which, together with the waveguiding properties, indicates their suitability for waveguide lasers.

Keywords: Liquid phase epitaxy; lithium yttrium fluoride; thin films; structure; morphology.

1. Introduction

Erbium ions (Er^{3+}) are known for their emission at ~2.8 μm falling into the mid-infrared spectral range [1-3]. Such emission is of practical importance for medicine (laser surgery), infrared countermeasures and sensing. It originates from the $^4I_{11/2} \rightarrow {}^4I_{13/2}$ Er^{3+} transition which has a self-terminating nature (the lifetime of the lower laser level is typically longer than that of the upper laser level). This dictates certain requirements for the host matrix (low phonon energies leading to weak non-radiative path), as well as the Er^{3+} doping level. Indeed, high doping levels promote the so-called energy-transfer upconversion process recycling the population of the lower laser level and allowing for continuous-wave laser operation [4].

Among the host materials studied for Er^{3+} doping to achieve ~2.8 μm emission, fluoride single crystals (e.g., $LiYF_4$ [2], CaF_2 [3], BaY_2F_8 [5], etc.) seem particularly suitable. They provide low phonon energies (446 cm^{-1} for $LiYF_4$ [6]), high available Er^{3+} doping levels and relatively long lifetimes of the $^4I_{11/2}$ and $^4I_{13/2}$ excited-states [7]. In addition, fluoride crystals offer good thermal properties (high thermal conductivity of 7.2 $Wm^{-1}K^{-1}$ along the ***c***-axis for undoped $LiYF_4$ [8]). Erbium-doped lithium yttrium fluoride (Er:$LiYF_4$) is known for generation of coherent ~2.8 μm light. Wyss *et al.* demonstrated laser emission at ~2.8 μm from a highly-doped (15 at.%) Er:$LiYF_4$ crystal with a record-high slope efficiency of 46% exceeding the Stokes limit [9]. Recently, Švejkar *et al.* demonstrated power scaling of an Er:$LiYF_4$ laser leading to multi-watt output at ~2.8 μm [10].

Waveguide (WG) lasers offer compact and integrated design, small mode areas and high intracavity light intensities. Mid-infrared WG lasers are of interest for sensing applications. One of the most common ways to produce planar WGs based on single-crystalline layers is Liquid Phase Epitaxy (LPE) [11,12] being a well-developed technology for $LiYF_4$ [12,13]. So far, single-crystalline oriented thin films of $LiYF_4$ doped with various rare-earth ions (RE^{3+}) such as Yb^{3+} [14], Tm^{3+} [15], Ho^{3+} [16], or Pr^{3+} [17] were grown on bulk undoped $LiYF_4$ substrates using LiF as a solvent. In these LPE experiments, relatively low propagation losses (down to 0.2 dB/cm at ~1 μm [14] and 0.11 dB/cm at ~2 μm [18]) were achieved. Efficient laser operation was demonstrated in RE^{3+}-doped $LiYF_4$ epitaxial films [14-17]. The possibility to incorporate RE^{3+} ions in high concentrations (at least up to 20 at.%) was proven in the case of Yb^{3+} [19] and Tm^{3+} [20] dopants.

To date, there are no reports on the fabrication of highly Er^{3+} doped $LiYF_4$ epitaxial layers featuring ~2.8 μm emission. Rogin and Hulliger described in general the growth of RE^{3+}-doped $LiYF_4$ epitaxial films with Nd^{3+} and Er^{3+} dopants at low concentrations (1 – 3 at.%) [12]. To enhance the refractive index contrast between the substrate and the layer, optically "passive" Gd^{3+} ions (~10 at.% in the melt) were added to the films. For this, (101) and (100) oriented $LiYF_4$ substrates were used. However, in [12], very little information was given about the Er:$LiYF_4$ films.

In the present work, we aimed to grow $LiY_{1-x}Er_xF_4$ and $LiY_{1-x-y}Er_xGd_yF_4$ films featuring high Er^{3+} doping levels on (001) oriented $LiYF_4$ substrates by LPE and to study the film structure, morphology and composition.

Previously, LPE was used to fabricate Er^{3+}-doped crystalline layers using other materials, e.g., $LiNbO_3$ [21], $KY(WO_4)_2$ [22,23] and $Yb_3Al_5O_{12}$ [24]. However, another prominent emission of Er^{3+} ions at ~1.5 μm was studied in these works. Er^{3+}-doped active WGs suitable for mid-infrared laser operation at ~2.8 μm were also fabricated by other methods, e.g., RF magnetron sputtering [25] and femtosecond direct laser writing [26].

2. Liquid Phase Epitaxy growth

Single-crystalline layers of $LiYF_4$ doped with Er^{3+} ions are grown on bulk substrates from undoped $LiYF_4$ by LPE. Lithium fluoride (LiF) is used as a solvent or as a self-flux compound by considering the initial composition of the growth batch, about 73 LiF – 27 YF_3 (mol%), i.e.,

relatively far from the $LiYF_4$ peritectic, about 51 LiF – 49 YF_3, see the phase diagram of the LiF – YF_3 binary system [27] in Fig. 1. It is selected to reduce the growth temperature and to prevent excessive vaporization of LiF at the expense of lower viscosity of the molten bath. Two compositions of the layer are studied, singly doped with 11 at.% Er^{3+} (composition #1) and codoped by 7 at.% Er^{3+}, 5 at.% Gd^{3+} (composition #2, for the concentrations in the bath). In both cases, Er^{3+} and Gd^{3+} ions are introduced to substitute the Y^{3+} cations. The Gd^{3+} cations are optically "passive", and they are added to enhance the refractive index contrast between the layer and the substrate.

The scheme of the LPE setup is described elsewhere [28]. It consists of a two-zone vertical tubular furnace and a quartz tube (the growth chamber). The crucible is placed inside the quartz tube in the furnace zone presenting the lowest vertical temperature gradient. On top of the growth chamber, a sample exchange chamber is positioned. It allows to exchange the samples and, if needed, to install a stirrer, and the two chambers are separated by an electro-valve. Both the growth and the sample exchange chambers are first sealed to high secondary vacuum and then refilled with Ar gas. The latter is done to avoid formation of unwanted oxyfluoride phases in the layers. During the growth, the use of the electro-valve allows us to preserve the proper temperature regime inside the growth chamber and to avoid its contamination, e.g., by water vapor.

The substrates for the LPE experiments are fabricated from bulk undoped $LiYF_4$ crystals grown by the Czochralski (Cz) method. The crystals are oriented using a Laue diffractometer (Thermo Scientific ARL EQUINOX) and the substrates are prepared with their plane being orthogonal to the [001] crystallographic axis. They are polished from both sides with good flatness ($\lambda/4$ in wave transmission), parallelism (about 10') and very low surface roughness (<2 nm). The latter is known to be critical for the growth of high optical quality RE^{3+}-doped $LiYF_4$ layers.

The reagents used are lithium fluoride LiF (Alfa-Aesar, 99.5% optical grade) and rare-earth oxides RE_2O_3 (RE = Y, Gd, Er, Alfa Aesar, 4N-REO). The oxide precursors are fluorinated following the procedure described in [19]. This is done to obtain the REF_3 (RE = Y, Gd, Er) reagents with higher purity than that for the commercial ones. The starting powders, 73 mol% LiF – 27 mol% REF_3 (with REF_3 taken according to the doping levels described above), are placed in a glassy carbon crucible. The total mass of the growth bath is 160 g. The crucible is placed in the growth chamber which is well degassed to a pressure of 10^{-4} mbar and then refilled with pure Ar. The growth charge is superheated ~20 °C above the expected liquidus temperature (~741 °C) and kept at this temperature for a few hours under mechanical stirring using an Inconel alloy-based stirrer leading to homogenization of the melt. Then, the temperature is slowly reduced towards the expected liquidus temperature, and the apparent onset of crystallization is determined in a series of test growth experiments using small (lateral size: 15 × 5 mm^2) substrates. The growth duration for the test experiments is 30 – 45 min. The layer growth / substrate dissolution is directly observed on a polished side surface of the test substrate using an optical microscope.

After the apparent onset of crystallization is determined, larger substrates (thickness: 3 mm, lateral size: 30 (height) × 11 (width) mm^2) were used. The growth is performed at well controlled supercooling (see below). The samples are placed vertically in the solution. During the growth, the sample is rotated at a speed of 10 rev / min in one direction. After the growth is completed, the sample is removed from the solution and slowly (during 20 - 40 min.) moved towards the sample exchange chamber. The sample is cooled to room temperature within minimum 1 hour. No annealing is applied to the as-grown epitaxies.

The side and top surfaces of the epitaxies are polished for further studies.

3. Characterization methods

The powder X-ray diffraction (XRD) patterns were obtained using a Bruker-AXS D8 Advance diffractometer with a vertical θ-θ goniometer. Soller slits of 2.5° for the incident and diffracted beams and a fixed 0.5° receiving slit were used. The measurements were carried out using CuK_α radiation obtained from a Cu X-ray tube. The diffractograms were recorded in the 2θ range of 5 - 80º, the angular step was 0.02° and the step time was 0.5 s.

For single-crystal XRD, we used a Bruker AXS D8 Discover diffractometer with a four-circle goniometer, a line focus Cu X-ray source, a Goebel mirror and an asymmetric Ge (220) double-bounce monochromator resulting in a parallel and monochromatic X-ray beam (Cu Kα1, λ = 0.15406 nm). A Ge (220) crystal analyzer was used as secondary optics. First, a 2θ-ω symmetric measurement was done in the range of diffraction angles 2θ = 15 - 80° with a step size of 0.01° and a step time of 0.5 s. In addition, the sample was tilted to reveal the (103) reflection. A symmetric measurement was done in the skew geometry in the 2θ range 30.0 – 30.6° with a step size of 0.002° and a step time of 0.5 s. A 2D map was obtained by taking a series of 2θ-ω at successive ω values and the DxTools viewer [29] was used for representation in the reciprocal space.

Differential Thermal Analysis (DTA) was performed using a TA Instruments SDT 2960 simultaneous DTA-TGA equipment. The measurements were carried out in platinum crucibles, using Al_2O_3 as a reference material. A 140 cm^3/min N_2 flow was applied to avoid formation of the oxyfluoride phase. The study was made in heating and cooling processes from 20 to 925 ºC. The rates of heating and cooling were 10 ºC/min, while the sample weight was ~10 mg.

To study the surface morphology of the as-grown epitaxial layers, we used an optical confocal microscope (Sensofar, S-neox) equipped with a blue light-emitting diode (λ = 405 nm) operating in the reflection mode.

The layers were also studied by Scanning Electron Microscopy (SEM) using a JCM-7000 NeoScope Benchtop microscope (Jeol) with an integrated Energy Dispersive X-ray (EDX) module. The accelerating voltage was 15 kV, the working distance was 13 mm and the measurements were performed in a high-vacuum mode.

The mid-IR luminescence spectra were measured using a 0.6 m monochromator (HRS2, Jobin-Yvon), a lock-in amplifier (SR810 DSP, Stanford Research Systems) and an InSb detector (J10D series, Judson Infrared) cooled by liquid N_2. The monochromator was purged by nitrogen. The system was calibrated using a Hg lamp (Schwabe).

4. Results and discussion

4.1. LPE growth

First, the apparent onset of crystallization was determined. It amounted to 746.0 °C and 746.6 °C (± 0.5 °C, for the batch compositions #1 and #2, respectively). These temperatures are slightly higher than those expected from the phase diagram for the LiF – YF_3 binary system proposed by Thoma *et al.* [27] (741 °C) which is assigned to the presence of ErF_3 in the composition. Fedorov *et al.* reported on higher melting temperature for $LiErF_4$ (840 °C) as compared to $LiYF_4$ (815 °C) [30]. The transition from growth to dissolution was observed within a range of ~1 °C.

Figure 2 presents the photographs of a clean substrate ($LiYF_4$) and an as-grown epitaxy (Er:$LiYF_4$ / $LiYF_4$) obtained using the batch composition #1. The growth temperature was 745.5 °C (an apparent supercooling of 0.5 °C) and the growth duration was 45 min. The film is clean and transparent, and it covers approximately 2/3 of the substrate. The growth meniscus contains a much thicker layer, and it is strongly covered by the crystallized solvent due to a thermal discontinuity related to the molten bath surface.

The effect of the apparent supercooling on the growth behavior of layers was studied using the batch composition #2, Fig. 3. For small supercooling of ~0.5 °C, the film is uniform and transparent. By increasing the supercooling to 1 – 2 °C, the growth rate increases, the

film surface exhibits anarchic crystallization, cracks propagating into the substrate and surface "ripples"; moreover, the deposition of solvent is enhanced. Finally, for large supercooling of ~6 °C, the layer becomes polycrystalline, and it is completely covered by solvent on the whole surface.

Thus, for further experiments, a supercooling of less than 1 °C was selected. The growth duration was in the range of 45 – 90 min. and the obtained layer thickness was 30 – 90 μm (on each side of the substrate) corresponding to a growth rate of 0.8 – 1.6 ± 0.5 μm/min. These values account only for the uniform thickness of the layer without the surface deposited solvent. The obtained growth rates agree with the data from Rogin *et al.* and indicate that the growth mechanism relies on the attachment of new building units anywhere at the layer edge [12].

We have also tested a growth regime when the substrate was first kept inside the solution maintained at higher temperature (760 °C) for a few min. resulting in healing imperfections on its surface with a subsequent growth at small supercooling (0.5 °C), Fig. 3. This greatly reduced the surface roughness of the layer. However, a certain curvature of the substrate / layer interface was observed due to the vertical thermal gradient in the melt. This method seems promising for substrates with tolerated polishing quality; however, further optimization of the high-temperature hold is needed.

For further characterizations, the surface deposited solvent could be easily removed by mechanical polishing.

4.2. Structure and thermal analysis

First, the material from the crystallized (upon its cooling) molten bath with the composition #2 was studied by powder XRD. Two types of materials were observed, namely, transparent rose-colored single crystals with a volume of a few mm^3 and white-colored translucent polycrystallites indicating a phase separation at the liquid state without stirring that occurs during cooling of the molten bath until it freezes at the solidification temperature. The XRD patterns, Fig. 4, indicate that transparent crystals have single-phase nature (tetragonal, $LiYF_4$-type structure with lattice constants a = 5.1704 Å and c = 10.7472 Å) and the translucent material is composed of LiF (29.4 wt%) with a cubic structure, a = 4.0304 Å and a similar $LiYF_4$-type phase (70.6 wt%). This composition agrees with the starting composition of the solution considering the possible evaporation of LiF and the relative uncertainty due to the non-uniformity of the phase separation.

The corresponding DSC curves are shown in Fig. 5. For the translucent material, Fig. 5(a), a single endothermic peak (onset temperature: T_{on} = 699 °C, peak temperature: T_p = 713 °C) corresponds to the eutectic temperature for the LiF – YF_3 diagram, cf. Fig. 1. The difference between this value and that indicated by Thoma *et al.* (695 °C) is probably due to the used composition with Er. Upon cooling, the onset of crystallization is observed at T_{on} = 744 °C in agreement with the LPE experiment. In the LPE setup, the temperature is measured by thermocouples positioned in the refractory wall of the furnace, very close to the side of the inner tube, i.e., the growth chamber [28]. For this purpose, there is a slight uncertainty of the absolute value of the temperature in the crucible, especially since there are convection fluxes in the melt. For the transparent crystals, the eutectic temperature is T_{on} = 698 °C and the melting point of the $LiREF_4$-type phase is T_{on} = 820 °C. It confirms our suggestion about the increase of the melting temperature for $Li(Y,Er,Gd)F_4$ as compared to pure $LiYF_4$.

The layers grown using the batch composition #1 with a clean surface were studied by high-resolution XRD, see Fig. 6. Considering the X-ray absorption by the $LiYF_4$ phase and its density, the depth probed during the XRD measurement was in the 5-30 μm range, less than the film thickness. Thus, mainly the diffraction from the film was measured. The layer exhibits only two intense diffraction peaks at 2θ = 33.36° and 70.08° both corresponding to (00*l*)

reflections of the $LiYF_4$ phase, namely, the (004) and (008) reflections, respectively, Fig. 6(a). This confirms good orientation of the film with respect to the substrate, i.e., the growth along the [001] direction. To determine the lattice constants for the layer, a high-resolution XRD pattern was also measured for a tilted geometry revealing the (103) diffraction peak, Fig. 6(b). A 2D map of this (103) reflection, Fig. 7, shows a thin intense node indicating a well-oriented layer without fluctuation of the lattice parameters. These measurements resulted in the average lattice constants for the tetragonal phase of a = 5.1696 Å and c = 10.7339 Å. A comparison of the XRD pattern of the layer with the standard one for undoped $LiYF_4$ indicates that the layer is isostructural to $LiYF_4$. It corresponds to the tetragonal crystal class (space group C^6_{4h} - $I4_1/a$, No. 88). It is difficult to determine a reliable value of the lattice mismatch between the layer and the substrate for batch #1 as it is within the error of calculation of the lattice constants.

The lattice constants for the Er:$LiYF_4$ and Er,Gd:$LiYF_4$ phases should be compared with those for undoped $LiYF_4$ (a = 5.164 Å and c = 10.740 Å [31]). In the $LiYF_4$ structure, there exists a single rare-earth site with S_4 symmetry and a VIII-fold fluorine coordination representing a slightly distorted dodecahedron [YF_8]. Both the Er^{3+} and Gd^{3+} cations are expected to replace for the Y^{3+} ones. The corresponding ionic radii are R_Y = 1.16 Å, R_{Er} = 1.14 Å and R_{Gd} = 1.20 Å [32]. The larger ionic radius of Gd^{3+} explains a slight increase of the lattice constants for the Er,Gd:$LiYF_4$ phase, the corresponding lattice mismatch with respect to the substrate is $\Delta a/a_{subst}$ = 0.12% and $\Delta c/c_{subst}$ = 0.07%.

The $LiYF_4$, $LiErF_4$ (a = 5.162 Å, c = 10.706 Å [33]) and $LiGdF_4$ (a = 5.225 Å, c = 10.987 Å [34]) crystals are isostructural (sp. gr. $I4_1/a$) and can form continuous solid solutions $LiY_{1-x-y}Er_xGd_yF_4$. A linear variation of the lattice constants is expected in this case. Thus, we obtain $\Delta a/a_{subst}$ = 0.04% and $\Delta c/c_{subst}$ = 0.06% for the codoped layer 6.9 at.% Er, 3.5 at.% Gd:$LiYF_4$ (batch #2) which reasonably agrees with the experimental values.

4.3. Layer topography

A typical confocal laser microscope image of the raw top surface of an Er:$LiYF_4$ thin film grown at 745.5 °C is shown in Fig. 8. The central part of the epitaxy was studied. It presents smooth clean areas of the film itself, as well as sharp surface deposited dendritic structures assigned to crystallization of the residual solvent (LiF). The surface of the film is not perfectly flat, but it presents irregular “hills” and “valleys”. Very similar growth behavior was observed before for other epitaxial fluoride films ($LiYF_4$ [19], CaF_2 [28]). The morphology is further revealed in the confocal observation mode using the confocal microscope, as shown in Fig. 9. The root mean square (rms) surface roughness is ~2 μm (compare with that for the polished substrates, a few nm). The spatial size of “hills” and “valleys” is about ~100 μm.

The surface roughness, as well as the remaining LiF on the surface is not critical for potential WG applications. Prior to WG experiments, the epitaxies are subjected to mechanical polishing of both the side and top surfaces. This is needed to precisely control the layer thickness for the desired modal behavior and simultaneously allows for reducing the scattering losses at the input and top surfaces.

The as-grown top and polished side surfaces of the Er:$LiYF_4$ film were further studied by SEM, Fig. 10. Figure 10(a) reveals polycrystalline LiF partially covering the surface of the film. Figure 10(b) shows one of the polished side faces. It reveals a clean and flat substrate / layer interface, a uniform and single-crystalline layer without secondary phases, inclusions or cracks, and a small surface deposition of LiF. The layer thickness is measured to be 40 ± 2 μm and it is uniform across the central part of the epitaxy.

The passive waveguiding properties of the polished Er:$LiYF_4$ / $LiYF_4$ epitaxy were confirmed by coupling a focused (using an aspherical lens with f = 40 mm) linearly polarized output of a Ti:Sapphire laser ($M^2 \approx 1$) tuned to 900 nm (out of Er^{3+} absorption) into the 30 μm thick layer. Using a short focal length (f = 15 mm) CaF_2 lens and a CCD camera, the near

field profile of the guided mode at the output facet of the WG was observed, representing a horizontal stripe profile (as there is no mode confinement in the plane of the layer). This mode behavior is typical for planar WGs.

4.4. Compositional analysis

The composition of the films was confirmed by EDX analysis. The EDX spectra of both the substrate ($LiYF_4$) and the layer (Er:$LiYF_4$) were measured, Fig. 11. Both spectra reveal the presence of host-forming elements (Y and F, Li is too light to be detected by EDX). Only in the spectrum of the layer, Er is clearly detected (Mα1, Lα1,2 and Lβ1,2 lines). Other impurity elements in small quantities are Si, O and C. The former two elements may originate from the silica tube, while C is a contamination probably coming from the glassy carbon crucible. The fraction of oxygen in the films is too low to cause the formation of an oxyfluoride phase, in agreement with the XRD findings.

EDX-based element mapping was applied to reveal the distribution of Y, Er and F elements over the polished side facet of the epitaxy, Fig. 12. The corresponding line element profiles across the layer are shown in Fig. 13(a). The Y content in the layer decreases with respect to the substrate while the Er content increases representing the $LiY_{1-x}Er_xF_4$ substitution. The F content is the same in the substrate and the layer indicating no deviation from the stoichiometry in the layer. The Er^{3+} ions are uniformly distributed in the layer. The upper limit for the substrate / layer interface, estimated from the element line profile of Y, is less than 1.5 μm.

A similar analysis was applied to the raw top surface of the epitaxy. The line element profiles of Y, Er and F were analyzed along a line crossing the surface dendritic structures, see Fig. 13(b). A strong enhancement of the F signal and a corresponding decrease of the Y and Er signals were detected for spatial positions corresponding to such structures. This clearly confirms that these structures contain no Y and Er elements and are composed of LiF.

The actual concentration of Er^{3+} ions in the layer was determined from optical absorption measurements using known absorption cross-sections for Er^{3+} ions in $LiYF_4$ [35]. For the 11 at.% Er:$LiYF_4$ layer (the starting composition), the actual doping level amounted to 10.8±0.7 at.% Er, so that the segregation coefficient for Er^{3+} ions, $K_{Er} = C_{layer}/C_{solution}$, where C is the doping level, was 0.98±0.06. Close to unity value of K_{Er} is due to the closeness of ionic radii of Y^{3+} and Er^{3+} ions for VIII-fold fluorine coordination (see above). The segregation coefficients for various RE^{3+} ions in $LiYF_4$ epitaxial films [15] are summarized in Fig. 14. They are plotted versus the ionic radius. According to the Onuma's principle, this dependence can be expressed using the following equation: $K_{RE} = 1 - C(R_{RE} - R_Y)^2$, where C is a material-dependent constant [36]. The points in Fig. 14 are well fitted using this dependence yielding $C = 58 \pm 5$ Å^{-2}. According to the previous study, $K_{Gd} = 0.70$, so that the actual doping levels for the layer grown using the batch composition #2 are 6.9 at.% Er, 3.5 at.% Gd.

The refractive index difference between the layer and the substrate, $\Delta n = n_{layer} - n_{substrate}$, can be estimated from the refractive indices of the parent compounds, $LiYF_4$, $LiErF_4$ and $LiGdF_4$. All these crystals are optically uniaxial (positive, $n_o < n_e$). For the films grown on (001) oriented $LiYF_4$ substrates, both principal light polarizations, π and σ (corresponding to the refractive indices n_e and n_o, respectively), are available for light propagating in the plane of the layer (i.e., in the WG configuration).

By using the following values (taken at ~1.06 μm, due to the data availability): $n_o = 1.4480$, $n_e = 1.4702$ ($LiYF_4$ [37]), $n_o = 1.466$, $n_e = 1.492$ ($LiErF_4$ [38]) and $n_o = 1.474$, $n_e = 1.502$ ($LiGdF_4$ [39]), we obtain $\Delta n_o = 1.9\times10^{-3}$ and $\Delta n_e = 2.4\times10^{-3}$ for the singly-doped epitaxy 10.8 at.% Er:$LiYF_4$ (batch #1) and $\Delta n_o = 2.2\times10^{-3}$ and $\Delta n_e = 2.6\times10^{-3}$ for the codoped one 6.9 at.% Er, 3.5 at.% Gd:$LiYF_4$ (batch #2). Here, we assumed a linear variation of the refractive index for the solid-solution $LiY_{1-x-y}Er_xGd_yF_4$. For the calculated values, it is clear that π-polarization (TM, in the WG geometry) provides higher refractive index contrast. Single Er^{3+} doping in high

concentrations (~10 at.% and above) provides relatively high Δ*n* values, so that Gd^{3+} codoping, which may increase the risk of layer fracture due to the stronger lattice distortion, is not necessary.

4.5. Mid-infrared luminescence

Mid-infrared luminescence in the layers was excited at 791 nm (to the $^4I_{9/2}$ Er^{3+} multiplet). The polarized luminescence spectra are shown in Fig. 15. The layers exhibit intense emission spanning from 2.65 to 2.9 μm related to the $^4I_{11/2} \rightarrow {}^4I_{13/2}$ transition of Er^{3+} ions. Higher luminescence intensity is observed for π-polarized light. The emission maximum is observed at ~2720 nm. The spectra do not change significantly with the addition of optically passive Gd^{3+} ions to the layers (batch #2).

The measured mid-infrared luminescence spectra are strongly polarized confirming the single-crystalline nature of the layers and their proper orientation.

5. Conclusions

To conclude, we report on the first highly Er^{3+}-doped (~7 – 11 at.%) $LiYF_4$ epitaxial layers. These layers, both singly doped and codoped with optically passive Gd^{3+} ions, are grown by LPE on (001) oriented bulk undoped $LiYF_4$ substrates using LiF as a solvent and a starting composition of 73 LiF – 27 REF_3 (mol%) providing reduced growth temperatures about 746 °C (as compared to compositions being closer to the peritectic one). The layers are single crystalline and well oriented. Selecting the proper apparent supercooling has a key effect on the growth behavior. When working at a supercooling of 0.5 – 1 °C, the formation of cracks and polycrystalline areas in the layer, as well as excessive solvent deposition on its surface are avoided. The growth rates in this case are about 0.8 – 1.6 ± 0.5 μm/min., resulting in layers with a thickness of 30 – 90 μm. A promising approach is the “healing” of the substrate surface by a short hold slightly above the liquidus temperature of the flux with a subsequent layer growth under small supercooling. The main challenge here is the proper control of the flatness of the layer / substrate interface.

The grown layers preserve the tetragonal structure (sp. gr. $I4_1/a$) and exhibit relatively low lattice mismatch with respect to the substrate. Er^{3+} doping in high concentrations (~10 at.% and above) is expected to provide enough refractive index contrast (about 2×10^{-3}) for potential waveguide applications, which eliminates the need of Gd^{3+} codoping. The latter, although being able to increase Δ*n* further, leads to higher lattice mismatch and provokes the formation of polycrystalline film areas. Due to the small difference of ionic radii of Er^{3+} and Y^{3+} cations, the segregation coefficient for Er^{3+} ions in the layers is close to unity, which makes it easy to control the actual doping level.

The developed Er^{3+}-doped layers exhibit intense polarized mid-infrared luminescence at ~2.8 μm, as well as waveguiding properties, making them promising for WG lasers.

Acknowledgements

This work was partially supported by the Spanish Government, Ministry of Science and Innovation (project No. PID2019-108543RB-I00), by the Generalitat de Catalunya (project No. 2017SGR755), the Agence Nationale de la Recherche (ANR-19-CE08-0028); “RELANCE” Chair of Excellence project funded by the Normandy Region and the “Investissements d’avenir” ANR-11-EQPX-0020. G.B. would like to thank Prof. Xavier Portier (CIMAP – ENSICAEN) for the access to the Scanning Electron Microscope.

References

1. R.C. Stoneman, L. Esterowitz, Efficient resonantly pumped 2.8-μm Er^{3+}:GSGG laser, Opt. Lett. 17 (1992) 816-818.

2. T. Jensen, A. Diening, G. Huber, B. H. T. Chai, Investigation of diode-pumped 2.8-μm Er:$LiYF_4$ lasers with various doping levels, Opt. Lett. 21 (1996) 585-587.
3. C. Labbe, J. L. Doualan, P. Camy, R. Moncorgé, M. Thuau, The 2.8 μm laser properties of Er^{3+} doped CaF_2 crystals, Opt. Commun. 209 (2002) 193-199.
4. M. Pollnau, T. Graf, J.E. Balmer, W. Lüthy, H.P. Weber, Explanation of the cw operation of the Er^{3+} 3-μm crystal laser, Phys. Rev. A. 49 (1994) 3990–3996.
5. M. Pollnau, W. Lüthy, H.P. Weber, T. Jensen, G. Huber, A. Cassanho, H.P. Jenssen, R.A. McFarlane, Investigation of diode-pumped 2.8-μm laser performance in Er:BaY_2F_8, Opt. Lett. 21 (1996) 48-50.
6. S.A. Miller, H.E. Rast, H.H. Caspers, Lattice vibrations of $LiYF_4$, J. Chem. Phys. 52 (1970) 4172–4175.
7. S. Hubert, D. Meichenin, B.W. Zhou, F. Auzel, Emission properties, oscillator strengths and laser parameters of Er^{3+} in $LiYF_4$ at 2.7 μm, J. Lumin. 50 (1991) 7-15.
8. R.L. Aggarwal, D.J. Ripin, J.R. Ochoa, T.Y. Fan, Measurement of thermo-optic properties of $Y_3Al_5O_{12}$, $Lu_3Al_5O_{12}$, $YAlO_3$, $LiYF_4$, $LiLuF_4$, BaY_2F_8, $KGd(WO_4)_2$, and $KY(WO_4)_2$ laser crystals in the 80–300 K temperature range, J. Appl. Phys. 98 (2005) 103514.
9. C. Wyss, W. Lüthy, H. P. Weber, P. Rogin, and J. Hulliger, Emission properties of an optimised 2.8 μm Er^{3+}:YLF laser, Opt. Commun. 139 (1997) 215-218.
10. R. Švejkar, J. Šulc, M. Němec, H. Jelínková, Compact diode-pumped CW and Q-switched 2.8 μm Er:YLF laser, J. Opt. Soc. Am. B 38 (2021) B26-B29.
11. B. Ferrand, B. Chambaz, M. Couchaud, Liquid phase epitaxy: A versatile technique for the development of miniature optical components in single crystal dielectric media, Opt. Mater. 11 (1999) 101-114.
12. P. Rogin, J. Hulliger, Liquid phase epitaxy of $LiYF_4$, J. Cryst. Growth 179 (1997) 551-558.
13. P. Rogin, G. Huber, J. Hulliger, $LiYF_4$ liquid phase epitaxy using an inverted slider geometry, J. Cryst. Growth 198-199 (1999) 564–567.
14. W. Bolaños, F. Starecki, A. Braud, J.-L. Doualan, R. Moncorgé, P. Camy, 2.8 W end-pumped Yb^{3+}:$LiYF_4$ waveguide laser, Opt. Lett. 38 (2013) 5377-5380.
15. P. Loiko, R. Soulard, G. Brasse, J.-L. Doualan, B. Guichardaz, A. Braud, A. Tyazhev, A. Hideur, P. Camy, Watt-level Tm:$LiYF_4$ channel waveguide laser produced by diamond saw dicing, Opt. Express 26 (2018) 24653-24662.
16. P. Loiko, R. Soulard, G. Brasse, J.-L. Doulan, A. Braud, A. Tyazhev, A. Hideur, P. Camy, Tm,Ho:$LiYF_4$ planar waveguide laser at 2.05 μm, Opt. Lett. 43 (2018) 4341-4344.
17. F. Starecki, W. Bolaños, A. Braud, J.-L. Doualan, G. Brasse, A. Benayad, V. Nazabal, B. Xu, R. Moncorgé, P. Camy, Red and orange Pr^{3+}:$LiYF_4$ planar waveguide laser, Opt. Lett. 38 (2013) 455-457.
18. W. Bolanos, F. Starecki, A. Benayad, G. Brasse, V. Ménard, J.-L. Doualan, A. Braud, R. Moncorgé, P. Camy, Tm:$LiYF_4$ planar waveguide laser at 1.9 μm, Opt. Lett. 37 (2012) 4032-4034 (2012).
19. G. Brasse, P. Loiko, C. Grygiel, A. Benayad, F. Lemarie, V. Zakharov, A. Veniaminov, J.L. Doualan, A. Braud, P. Camy, Liquid Phase Epitaxy growth, structure and spectroscopy of highly-doped 20 at.% Yb^{3+}:$LiYF_4$ thin films, J. Lumin. 236 (2021) 118071.
20. R. Soulard, M. Salhi, G. Brasse, P. Loiko, J.-L. Doualan, L. Guillemot, A. Braud, A. Tyazhev, A. Hideur, P. Camy, Laser operation of highly-doped Tm:$LiYF_4$ epitaxies: towards thin-disk lasers, Opt. Express 27 (2019) 9287-9301.
21. J.B. Shim, N. Yoshimoto, M. Yoshizawa, D.H. Yoon, Structural characteristics of Er doped $LiNbO_3$ thin films grown by the liquid phase epitaxy method, Cryst. Res. Technol. 36 (2001) 1209-1214.
22. W. Bolaños, J.J. Carvajal, X. Mateos, M.C. Pujol, N. Thilmann, V. Pasiskevicius, G. Lifante, M. Aguiló, F. Díaz, Epitaxial layers of $KY_{1-x-y}Gd_xLu_y(WO_4)_2$ doped with Er^{3+} and Tm^{3+} for planar waveguide lasers, Opt. Mater. 32 (2010) 469-474.

23. S.A. Vázquez-Córdova, S. Aravazhi, C. Grivas, Y.-S. Yong, S.M. García-Blanco, J.L. Herek, M. Pollnau, High optical gain in erbium-doped potassium double tungstate channel waveguide amplifiers, Opt. Express 26 (2018) 6260-6266.
24. T. Hlásek, K. Rubešová, V. Jakeš, P. Nekvindová, M. Kučera, S. Daniš, M. Veis, V. Havránek, Structural and waveguiding characteristics of Er^{3+}:$Yb_3Al_{5-y}Ga_yO_{12}$ films grown by the liquid phase epitaxy, Opt. Mater. 49 (2015) 46-50.
25. V. Nazabal, F. Starecki, J.L. Doualan, P. Němec, P. Camy, H. Lhermite, L. Bodiou, M.L. Anne, J. Charrier, J.L. Adam, Luminescence at 2.8 μm: Er^{3+}-doped chalcogenide micro-waveguide, Opt. Mater. 58 (2016) 390-397.
26. Q. Tian, P. Yin, T. Zhang, L. Zhou, B. Xu, Z. Luo, H. Liu, Y. Ge, J. Zhang, P. Liu, X. Xu, MXene $Ti_3C_2T_x$ saturable absorber for passively Q-switched mid-infrared laser operation of femtosecond-laser–inscribed Er:Y_2O_3 ceramic channel waveguide, Nanophoton. 9 (2020) 2495-2503.
27. R.E. Thoma, C.F. Weaver, H.A. Freidman, H. Insley, L.A. Harris, H.A. Yakel, Phase equilibria in the system LiF–YF_3, J. Phys. Chem. 65 (1961) 1096–1099.
28. G. Brasse, P. Loiko, C. Grygiel, P. Leprince, A. Benayad, F. Lemarie, J.L. Doualan, A. Braud, P. Camy, Liquid Phase Epitaxy growth of Tm^{3+}-doped CaF_2 thin-films based on LiF solvent, J. Alloy Compd. 803 (2019) 442-449.
29. A. Boulle, DxTools: processing large data files recorded with the Bruker D8 diffractometer, J. Appl. Cryst. 50 (2017) 967-974.
30. P.P. Fedorov, B.P. Sobolev, L.V. Medvedeva, B.M. Reiterov, Revised phase diagrams of LiF-RF_3 (R = La-Lu, Y) systems, In *Growth of Crystals* (Springer, Boston, MA, 2002), pp. 141-154.
31. E. Garcia, R.R. Ryan, Structure of the laser host material $LiYF_4$, Acta Cryst. C49 (1993) 2053-2054.
32. A.A. Kaminskii, *Laser crystals: their physics and properties* (Springer, 2013).
33. J.S. Abell, I.R. Harris, B. Cockayne, A study of the $LiYF_4$-$LiErF_4$ psuedo-binary system, J. Mater. Sci. 12 (1977) 670-674.
34. I.M. Ranieri, A.H.A. Bressiani, S.P. Morato, S.L. Baldochi, The phase diagram of the system LiF–GdF_3, J. Alloys Compd. 379 (2004) 95-98.
35. S.A. Payne, L.L. Chase, L.K. Smith, W.L. Kway, W.F. Krupke, Infrared cross-section measurements for crystals doped with Er^{3+}, Tm^{3+} and Ho^{3+}, IEEE J. Quantum Electron. 28 (1992) 2619-2630.
36. K. Subbotin, P. Loiko, S. Slimi, A. Volokitina, A. Titov, D. Lis, E. Chernova, S. Kuznetsov, R.M. Solé, U. Griebner, V. Petrov, M. Aguiló, F. Díaz, P. Camy, E. Zharikov, X. Mateos, Monoclinic zinc monotungstate Yb^{3+},Li^{+}:$ZnWO_4$: Part I. Czochralski growth, structure refinement and Raman spectra, J. Lumin. 228 (2020) 117601.
37. N.P. Barnes, D.J. Gettemy, Temperature variation of the refractive indices of yttrium lithium fluoride, J. Opt. Soc. Am. 70 (1980) 1244-1247.
38. V. Vasyliev, E.G. Villora, M. Nakamura, Y. Sugahara, K. Shimamura, UV-visible Faraday rotators based on rare-earth fluoride single crystals: $LiREF_4$ (RE = Tb, Dy, Ho, Er and Yb), PrF_3 and CeF_3," Opt. Express 20 (2012) 14460-14470.
39. M.J. Weber, *Handbook of optical materials* (CRC press, 2018).

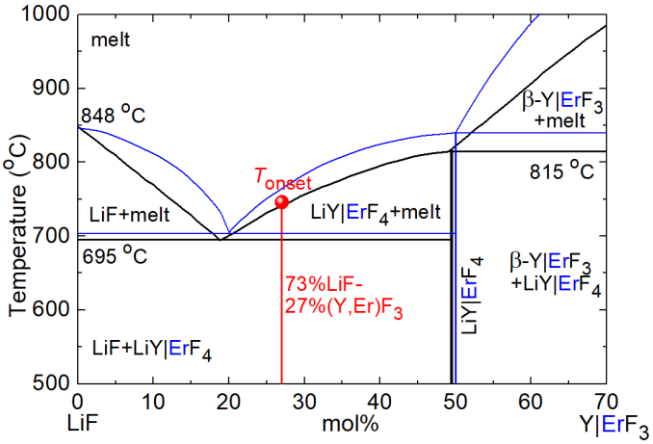

Figure 1. Phase diagram of the LiF – YF_3 (*black*) and LiF – ErF_3 (*blue*) binary systems (according to our data and [27,30]), *bold black line* - the $LiYF_4$ peritectic, *red line* - the composition selected for the LPE growth, *red circle* – apparent onset of crystallization. The indicated temperatures correspond to the LiF – YF_3 diagram.

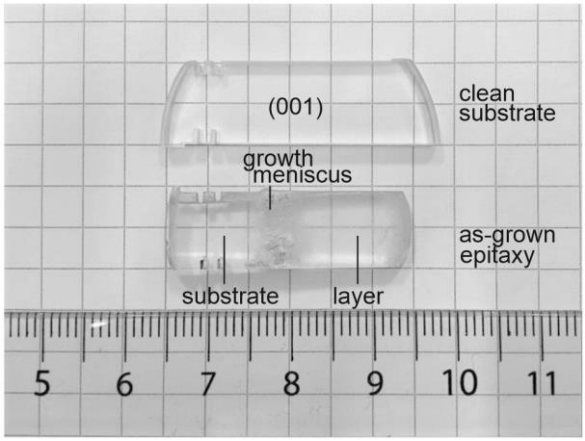

Figure 2. Photograph of the as-grown Er:$LiYF_4$ / $LiYF_4$ epitaxy grown at 745.5 °C for 45 min. and (001)-oriented $LiYF_4$ substrate.

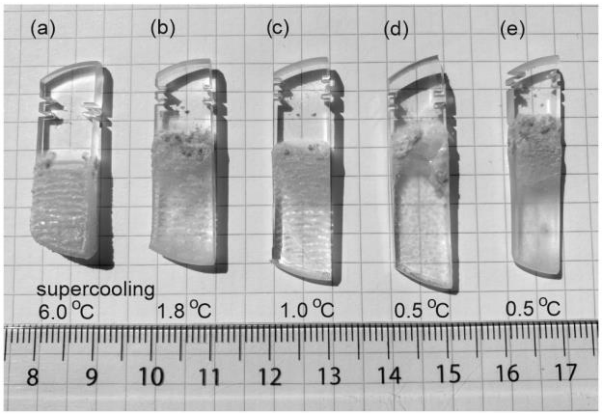

Figure 3. Effect of the apparent supercooling on the growth behavior of Er,Gd:$LiYF_4$ layers on (001)-oriented $LiYF_4$ substrates: the supercooling is (a) 6.0 °C, (b) 1.8 °C, (c) 1.0 °C, (d) 0.5 °C (direct growth) and (e) 0.5 °C (growth after pre-dissolving the substrate at 760 °C during 5 min). The growth duration is 45 min.

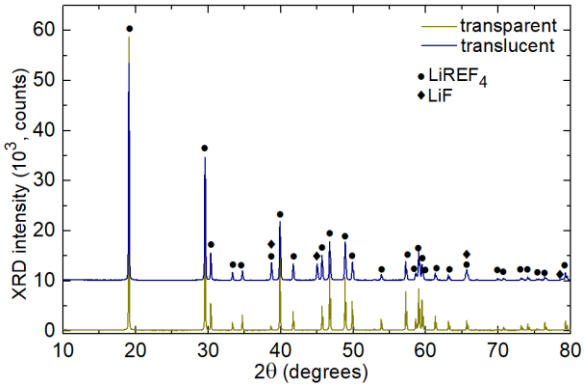

Figure 4. Powder X-ray diffraction (XRD) patterns of the crystallized molten bath of the LPE experiment: translucent polycrystalline material and transparent rose-colored single crystals.

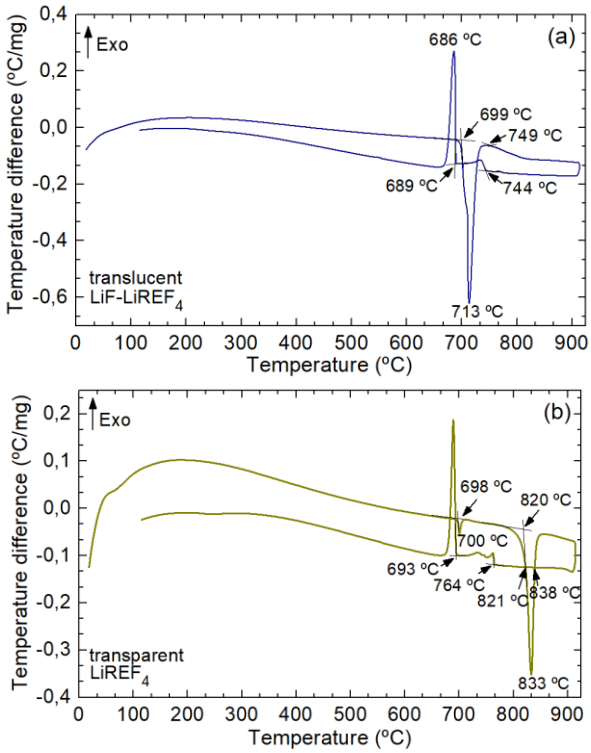

Figure 5. Differential thermal analysis curves for the crystallized molten bath of the LPE experiment: (a) translucent polycrystalline material; (b) transparent rose-colored $LiREF_4$ crystals.

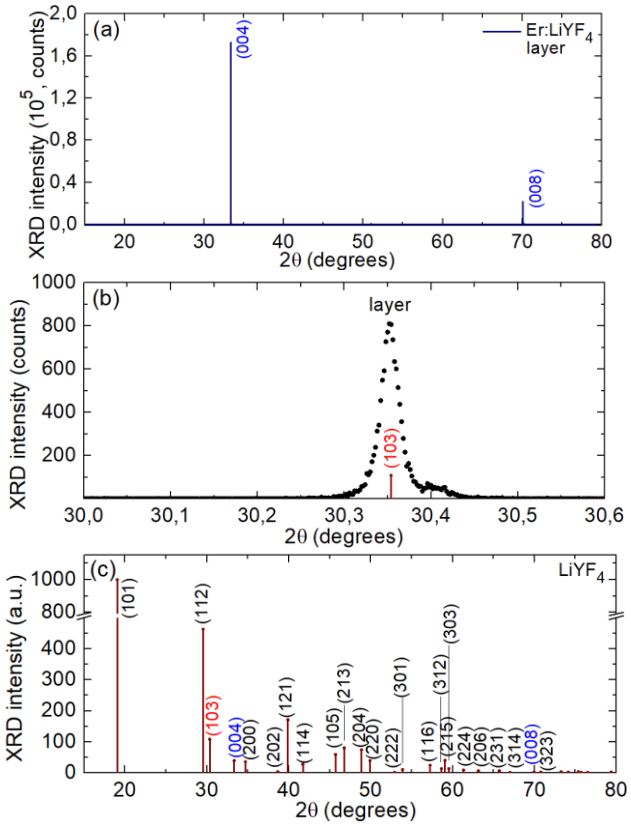

Figure 6. High resolution X-ray diffraction (XRD) study of the Er:$LiYF_4$ / $LiYF_4$ epitaxy: (a,c) measured XRD patterns of the layer, symmetric 2θ - ω scans: (a) standard sample orientation and (b) tilted sample in skew geometry revealing the (103) reflection; (c) standard pattern of undoped $LiYF_4$ (ICSD card No. 02-7896), *numbers* indicate the Miller's indices, (*hkl*).

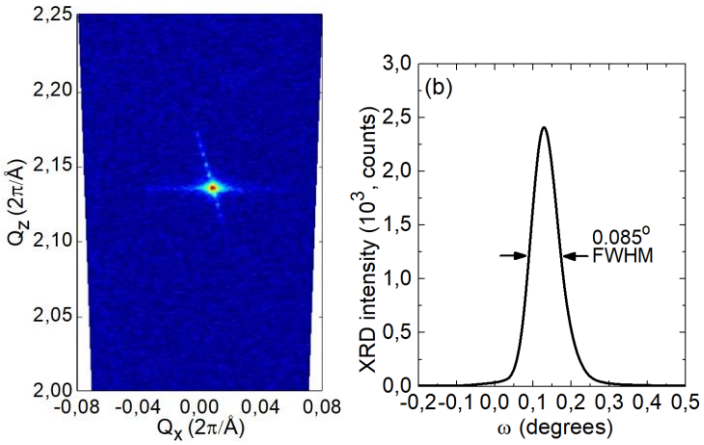

Figure 7. (a) Reciprocal space mapping of the (103) node for the Er:$LiYF_4$ layer; (b) the rocking curve of this node.

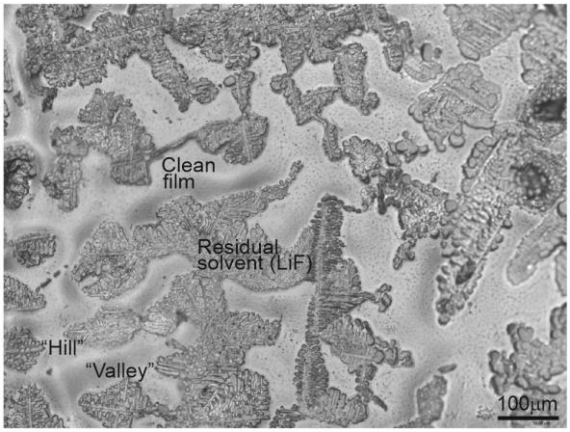

Figure 8. Confocal laser microscopy image of the top surface of as-grown Er:$LiYF_4$ thin film. Microscope objective 20×, bright field, reflection mode, λ = 405 nm.

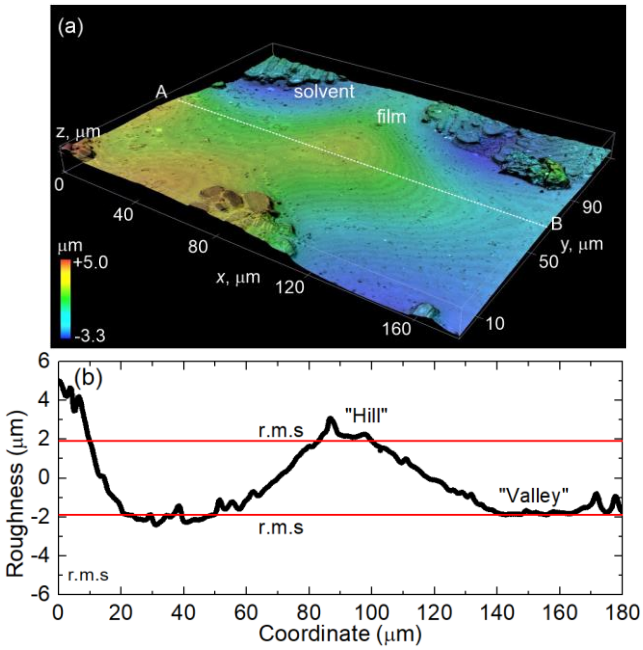

Figure 9. Surface topography of the as-grown Er:$LiYF_4$ thin film: (a) 3D plot, (b) surface roughness plot along the A – B line, rms – root mean square deviation.

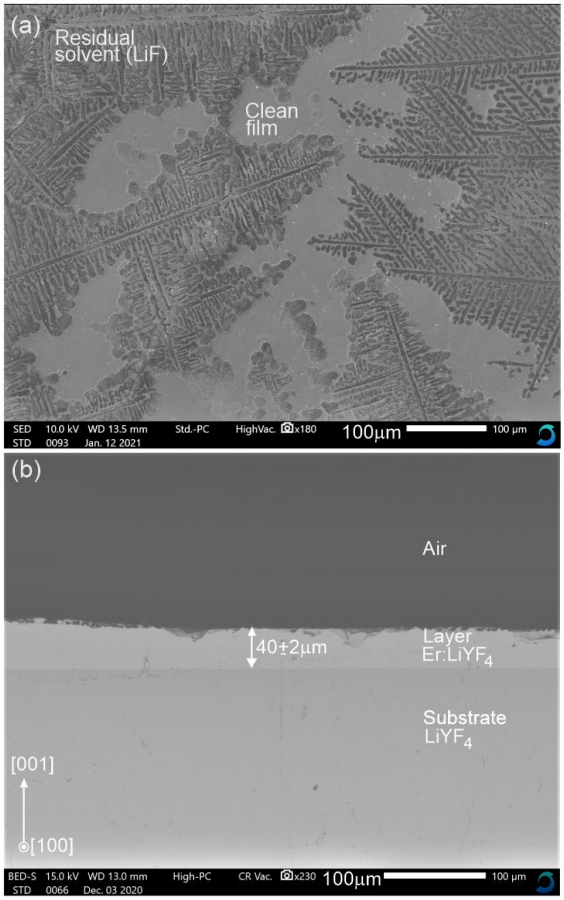

Figure 10. (a,b) Scanning Electron Microscope (SEM) images of (a) the as-grown top surface and (b) polished end-facet of the Er:$LiYF_4$ / $LiYF_4$ epitaxy.

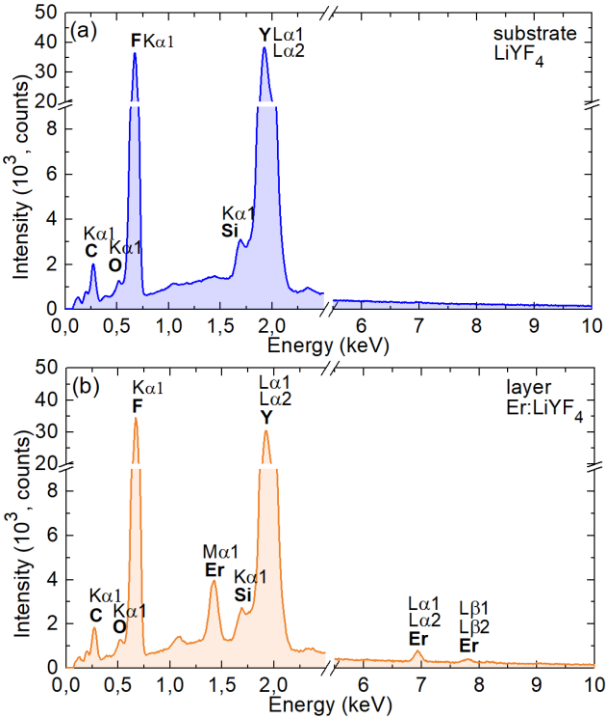

Figure 11. Energy-dispersive X-ray (EDX) spectra of the Er:$LiYF_4$ epitaxial layer and the $LiYF_4$ substrate (measured in the lateral geometry).

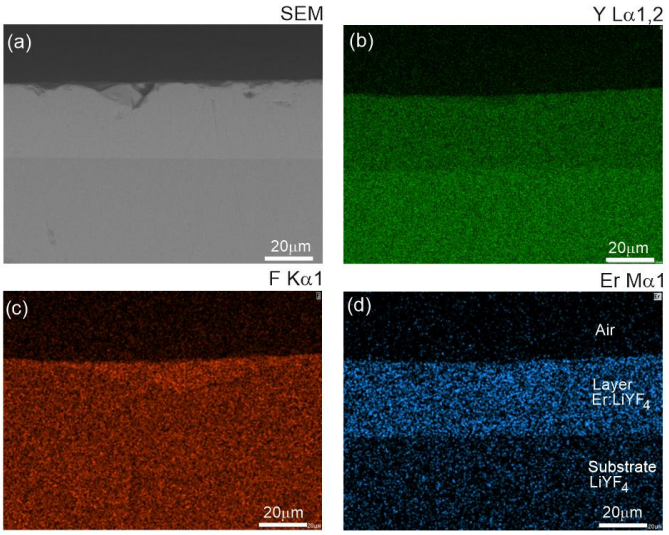

Figure 12. Element mapping for the Er:$LiYF_4$ / $LiYF_4$ epitaxy (lateral geometry): (a) SEM image, (b-d) element maps: (b) Y Lα1,2, (c) F Kα1 and (d) Er Mα1.

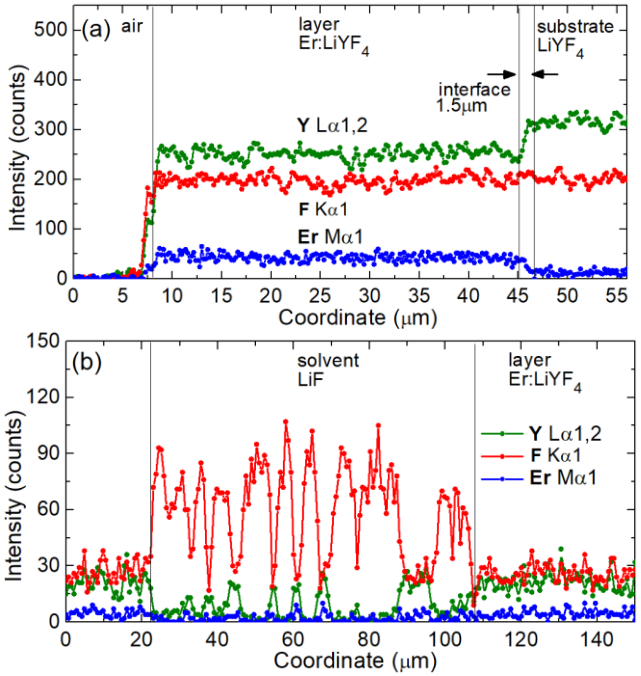

Figure 13. Element line profiles for the Er:$LiYF_4$ / $LiYF_4$ epitaxy: (a) across the polished side face, A' – B' line, Fig. 10(b); (b) along the raw top surface, A" – B" line, Fig. 10(a).

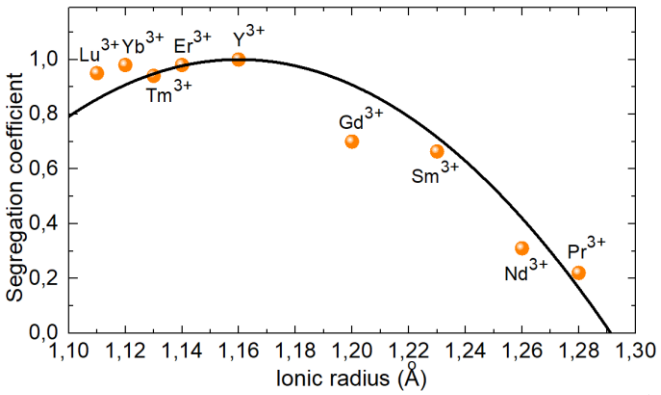

Figure 14. Segregation coefficient of the rare-earth ions, RE^{3+} in $LiYF_4$ epitaxial films as a function of their ionic radii for VIII-fold fluorine coordination: *symbols* – experimental data ([15] and this work), *curve* – their parabolic fit (see explanations in the text).

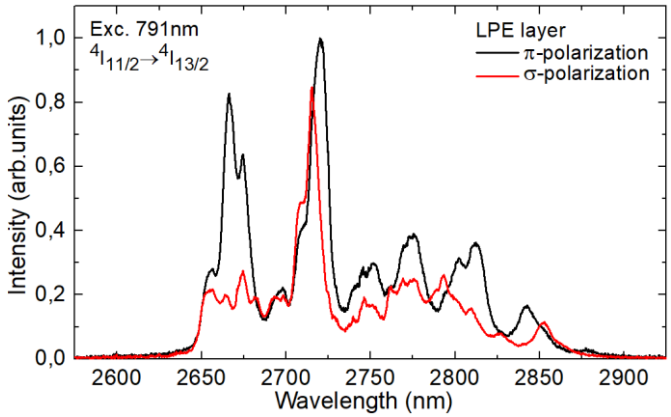

Figure 15. Polarized mid-infrared luminescence spectra of Er^{3+} ions from the Er:$LiYF_4$ epitaxial layer, λ_{exc} = 791 nm. The light polarizations are π and σ.